GEOLOGY

Predicting the preservation of buried ore deposits using deep-time landscape evolution modeling

Addison Tu[1]*, Sabin Zahirovic[1], Sara Polanco[1,2], Samuel C. Boone[1], Matt Boyd[1,3], Claire Mallard[1], Pedro Restrepo[4], Youseph Ibrahim[5], Luke Mahoney[6], Tristan Salles[1], Brent McInnes[7], Ehsan Farahbakhsh[1], Fabian Kohlmann[8], Maria Seton[1], Dietmar R. Müller[1]

Porphyry copper discoveries are declining despite rising demand to meet net-zero targets, highlighting the need for innovative exploration strategies. While many advances have focused on ore formation at depth, a major challenge remains in understanding how erosion and uplift over millions of years affect deposit preservation. These postmineralization processes determine whether porphyry systems are exposed, buried, or eroded entirely. We present a physically based landscape evolution model that incorporates spatially variable erodibility, dynamic uplift histories, climate and sea level change, and evolving topography over geological timescales. This richer input data, combined with tighter calibration, enables quantification of preservation potential and marks a step beyond prior conceptual and time-static models. We apply the model to New Guinea's geologically complex mountains and integrate it with machine learning–derived ore formation probabilities. The combined model predicts known porphyry endowment, identifies new targets, and constrains preservation likelihood, validating this open-source method as a flexible and affordable exploration tool in dynamic tectonic settings.

INTRODUCTION

Building a sustainable future will require more metals than ever, driven by the need to roll out green energy technologies to achieve low-carbon infrastructure (*1*–*3*). Matching this demand for strategic and critical minerals will likely require the discovery of new ore deposits. However, these discoveries are increasingly rare because of the depletion of near-surface deposits, which reduces the effectiveness of traditional, surface-based exploration techniques. This necessitates the development of more efficient techniques to find ore deposits situated at depth. Several approaches exist to assess the likelihood of ore deposit formation over time and are often combined, including geological mapping (*4*–*8*), geochemistry (*4*–*6*, *8*, *9*), geophysics (*5*, *8*, *10*, *11*), thermomechanical models (*11*, *12*), and machine learning models (*13*–*16*). However, these predictions often lack explicit consideration of ore deposit preservation, which encompasses events between the timing of ore formation and the present day and can span many millions of years. An ore deposit formed at depth may undergo burial because of sediment deposition or deformation or, conversely, undergo exhumation from erosion or tectonic exhumation. Given sufficient exhumation, the ore deposit may be brought to the surface and then eroded, destroying the original deposit, and the ore may be redeposited. This might necessitate exploration for sediment-hosted ore deposits downstream, which would require an understanding of ancient source-to-sink histories.

We present an advanced method to assess the exhumation and preservation of porphyry copper deposits using landscape evolution modeling (see full details in Materials and Methods). Unlike previous conceptual studies that largely rely on time-invariant or static conditions (*17*), our approach explicitly simulates erosion, uplift, and sedimentation over millions of years, accounting for time-evolving climate, surface processes, and spatially variable erodibility. We test our approach on the mountains of New Guinea and target porphyry copper deposits over the past 15 million years (Myr), using a published machine learning model (*15*), to provide ore deposit formation predictions and a newly developed Badlands (*18*) landscape evolution model to assess preservation potential. The model was calibrated against empirical constraints on present-day topography (*19*) and sediment accumulation (see Materials and Methods) using a statistical experimental design framework (*20*, *21*). This allowed simultaneous tuning of 22 parameters across more than 2300 simulations. Our approach enables spatiotemporal prediction of ore deposit preservation, providing insights into how postmineralization processes control the present-day accessibility of mineral systems.

New Guinea is an ideal test case due to its dynamic landscape and high prospectivity arising from a prolonged history of subduction-related volcanism and related porphyry mineralization (Fig. 1) (*22*, *23*). The mountains feature some of the highest rates of uplift (*24*–*26*) and erosion (up to 2 km/Myr) (*26*–*29*) on the planet, presenting a natural extreme of landscape change and rapid exhumation of ore deposits (*28*, *30*), and subsequent destruction with potential redeposition downstream. The orogen has a young (15 Myr) and relatively well-constrained geological history (*22*, *24*, *31*–*33*), which substantially reduces model uncertainty (*34*) and enables improved calibration of spatiotemporal modeling constraints. For example, the past 15 Myr have better temporal resolution of tectonic (*24*, *35*, *36*) and sea level (*37*) reconstructions, as well as enhanced preservation of geological evidence.

Our preferred Badlands (*18*) landscape evolution simulation was the product of over 2300 model runs and 22 calibrated parameters (Table 1). To capture the vast number of processes contributing to mountain belt development and evolution, we incorporated relevant aspects attributed to the deep Earth, surface, hydrosphere, and atmosphere (Fig. 1A). We included three deep Earth processes:

---

[1] School of Geosciences, The University of Sydney, Sydney, New South Wales, Australia. [2] School of Environmental and Life Sciences, The University of Newcastle, Newcastle, New South Wales, Australia. [3] Geological Survey of Victoria, Melbourne, Victoria, Australia. [4] EGRS Petronas, Kuala Lumpur, Malaysia. [5] Department of Geology & Geophysics, Texas A&M University, College Station, TX 77843, USA. [6] Geological Survey of New South Wales, Sydney, New South Wales, Australia. [7] John de Laeter Centre, Curtin University, Perth, Western Australia, Australia. [8] Lithodat Pty. Ltd., Melbourne, Victoria, Australia.
*Corresponding author. Email: addison.tu@sydney.edu.au

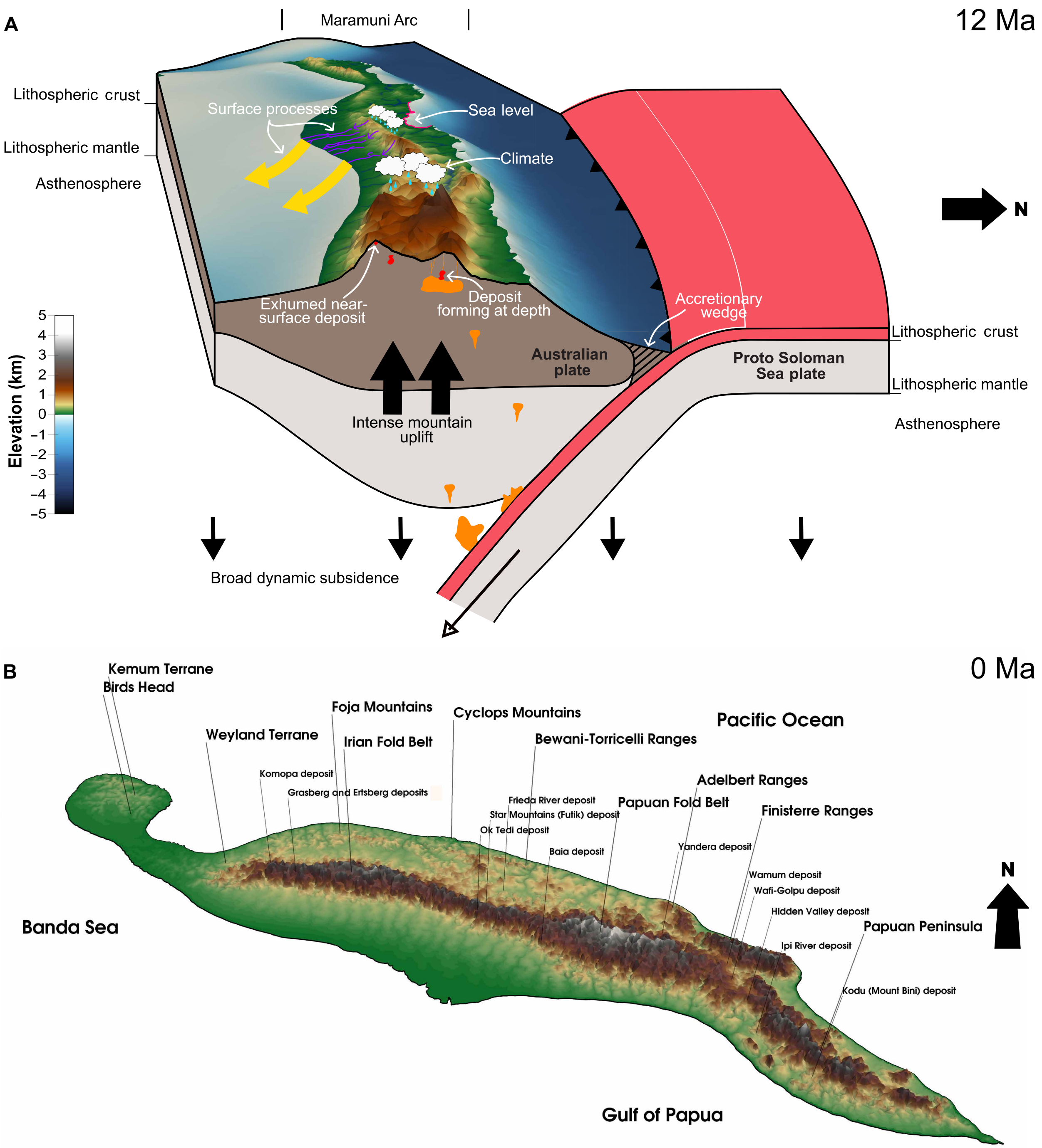

Fig. 1. Simplified depiction of the modeled processes and topography of the preferred model at the present day. (**A**) Schematic of the simulated processes spanning deep Earth to the atmosphere, using a section of the modeled Miocene (~12 Ma) Maramuni Arc topography. Localized uplift is depicted to arise from convergence between the subducting Proto Solomon Sea and overriding Australia plates. The uplift causes the development of the mountain ranges, and surface processes act to move material from higher to lower elevations. Porphyry copper ore deposits are schematically depicted in red, illustrating ore deposit formation associated with volcanism and subsequent exhumation of ore deposits toward the surface by erosional denudation of the mountain ranges. (**B**) High-angle three-dimensional perspective of the New Guinea topography, from the preferred model at present day with key areas annotated. Deposit locations are also provided in table S1.

Table 1. Parameters explored throughout model calibration. A comprehensive list of explored parameters and the final values implemented in the preferred model. Parameters that have no initial values were not implemented in the earliest experiment sets and introduced in later experiments sets. Uniform erodibility refers to a single erodibility value used across the entire model domain, and nonuniform erodibility refers to the global relative erodibilities based on surface lithology that are multiple by a factor, referred to as the "base erodibility" for calibrated implementation into Badlands. The methodology for the timing and calibration of imposed uplift is described in the "Imposing periods of uplift" section.

Parameter		Description	Initial value(s)	Explored values	Preferred model (model 26-5)
Erodibility		Erodibility of the strata	Uniform erodibility: $(2-6)\times 10^{-6}$	Uniform erodibilities: 1×10^{-7}–1×10^{-4} Nonuniform erodibilities with base erodibilities: 2×10^{-5} –6×10^{-5}	Nonuniform erodibilities with base erodibility: 3×10^{-5}
Tectonic		Imposed tectonic uplift	Arbitrary values	Continued refinement of differential uplift magnitudes throughout calibration and parameter exploration	See the "Imposing periods of uplift" section
n		Slope exponent in fluvial erosion model	1	0.7–1.2	0.8
m:*n* ratio		The value *m* relative to the value of *n*	0.5	0.4–0.6	0.5
modeltype		Fluvial erosion model	Detachment limited	Detachment-limited, transport-limited (tool and cover)	Transport-limited (tool and cover)
Transport-limited (tool and cover) fluvial erosion parameters	*kt*	Channel sediment erodibility	–	0.0001–0.008	0.0004
	mt	Discharge exponent for transport-limited regime	–	1.4–1.6	1.4
	nt	Slope exponent for transport-limited regime	–	1	1
	b	Power law relation between channel width and discharge	–	0.4–0.6	0.4
	mp	Exponent affecting erodibility dependence on precipitation	–	0	0
	bedslp	Bedload (bedload affects the ability to incise) slope dependency	–	0 (no effect), 1 (linear), 2 (exponential), and 3 (logarithmic)	1(linear)
Marine parameters	*cmarine*	Diffusion coefficient of marine sediments	2	0.001–1000	500
	diffprop	Percentage of sediment transported downstream during a time step	0.008–0.2	0.001–0.999	0.9
	diffnb	Number of steps to distribute sediment downstream during a time step	5	2–20	12
	propa	Scaling parameters for slope-dependent diffprop	–	1000–8000	6000
	propb		–	0.00001–0.01	0.0005
	criver	Diffusion of river-derived marine sediments	10	2–100	10

(*Continued*)

(*Continued*)

Parameter		Description	Initial value(s)	Explored values	Preferred model (model 26-5)
Additional terrestrial surface processes	*slp_{cr}*	Critical slope to force alluvial plain deposition	0.001	0.0001–0.01	0.01
	perc_dep	Maximum deposition (%) in alluvial plain during a time step	0.75	0.5–1.0	0.75
	caerial	Hillslope diffusion coefficient	1	0.0001–10	0.0001
elasticH		Lithospheric elastic thickness (m)	24, 000	20,000–28,000	28, 000
curve		Sea level curve	Miller (2020) short term	Miller (2020) short term, Haq (1987) long term	Miller (2020) short term

dynamic topography associated with mantle convection (*24*), uplift associated with tectonic convergence (Table 2), and the coupled gFlex (*38*) model to capture lithospheric flexural isostatic uplift and subsidence responses, related to erosional unloading and depositional loading, respectively. Surface processes accounted for in the Badlands model included fluvial erosion, transport, and sediment deposition using a transport-limited stream power law, marine transport (*18*), and hillslope diffusion (*18*). Surface processes were also influenced by spatially varying erodibility based on surface lithology (*39*). The hydrospheric and atmospheric system forcings were captured by integrating a temporally evolving sea level model (*37*) and a temporally and spatially variable paleoprecipitation model (*40*). The calibration of such a vast number of parameters was done iteratively using a design of experiments approach (*20*, *21*). Several parameters were introduced throughout the iterations, where, in each iteration, hundreds of models were generated with varied combinations of parameter values. The models were then computed and tested against sediment thickness grids and the Earth Topography (ETOPO) Global Relief Model (*19*), where the best combinations were brought forward to the next iteration when further parameters were introduced and calibrated.

To assess the preservation of potential ore deposits, we require prior predictions for emplacement at depth. We use a published machine learning model to provide predictions of ore deposit emplacement at depth (*15*), where the depth of emplacement is assumed to be between 2 and 3.25 km (see Materials and Methods). This machine learning model is well suited because the predictions are spatiotemporal, and the predictions cover all New Guinea for the 15- to 0-millon years ago (Ma) time frame. Furthermore, the machine learning model and our landscape evolution model share identical tectonic histories (*24*, *35*). The emplacement predictions are provided as relative probabilities for deposit formation at 1-Myr intervals. The machine learning model was trained using kinematic data from plate reconstructions with the location and formation age of known ore deposits (*15*) [for more details, refer to Farahbakhsh *et al.* (*15*)]. Notably, where available, alternative mineral ore deposit emplacement models can be used with our approach.

RESULTS

Mountain range development and evolution

The preferred landscape evolution model provides quantitative estimates of erosion, uplift, and paleoelevation that align well with empirical observations. When compared to the topography dataset (Fig. 1A), the model achieved a root mean square error (RMSE) of 1100.42 m across the entire domain and 668.95 m within highland regions (>600-m elevation) (Fig. 2C). It also reproduced 70.73% of the depositional volume recorded in 15- to 0-Ma sediment data from the Gulf of Papua.

Here, we define net uplift as the summation of imposed tectonic uplift (U_{tectonic}) and isostatic flexural rebound due to erosional unloading (or subsidence where sediments are deposited) (U_{flexure}). Dynamic topography was excluded from the net uplift calculations, as its influence on mountain uplift was negligible (~250 m of dynamic subsidence over 15 Myr), compared to flexural unloading and imposed tectonic uplift.

The initial topography is a revised paleogeographic map (see Materials and Methods) at 15 Ma (Fig. 2). The topography features the Maramuni Arc, characterized by the narrow NW-SE trending region of low topography, with some moderately elevated (~1000 m) areas in the east (*41*). The elongated island at the Bird's Head is proposed to have formed in response to the initiation of folding and inversion (*41*), arising from highly oblique convergence along the northern margin of the Australian plate (*24*).

A documented 15- to 6-Ma period of uplift was imposed in the model along the Maramuni Arc, which is widely attributed to oblique convergence between the Proto Solomon Sea plate and the Australian plate (*24*, *31*, *33*). Model predictions show that the topographic expression of the resulting uplift was focused in the east, where more extensive highlands developed and uplift rates reached up to 1.5 km/Myr (movie S3). Field-based (*42*, *43*) and thermochronological (*28*) observations indicate that erosion of the uplifted arc was focused on both northern and southern flanks, causing cutback of the mountains. By 7 Ma, the landscape evolution model predicts that peaks of up to 4.5 km emerged out of the broader plateau in the eastern region of the arc and that maximum total erosion reached ~6.0 km, with upper

Table 2. The timing of imposed uplift events and corresponding evidence. The timing of uplift was based on external evidence for each region in Fig. 5. Where available, thermal history models of thermochronology data were the preferred line of evidence for calibrating uplift in the landscape evolution model, and justification is provided for attributing modeled cooling to exhumation. Thermochronological systems included are (U-Th)/He in apatite (AHe), apatite fission track (AFT), (U-Th)/He in zircon (ZrHe), zircon fission track (ZrFT), and K-Ar in hornblende and biotite (K-Ar). Other sources of data were implemented for the remaining regions and are outlined in the final column.

Region	Uplift timing (Ma)	Based on thermochronology	Thermal model data		Alternative lines of evidence for timing of uplift
			Justification for attributing cooling to exhumation	Fig. 6	
Papuan and Irian Fold Belts	7–0	AHe, AFT, ZrHe, and sediment deposition constraints (*72*)	Outcrops of Darai Limestone at elevations up to 3 km. Marine limestone deposition occurred from late Oligocene to late Miocene (*48*, *72*, *77*, *78*).	A	–
West Papuan Fold Belt	7–0	AHe, AFT, and ZrHe (*72*)			–
Mobile Belt	15–6	AFT (*33*)	The exposure of the Miocene-aged Akuna and Bismarck Intrusive Complexes supports Miocene erosion (*22*, *33*, *71*).	B	–
	6–0	AFT (*33*)	Outcrops of the Omung Metamorphics intruded by the 244-Ma Kubor Granodiorite (*79*) at elevations of >1.5 km. However, in adjacent regions, these units are covered by >3 km of younger Mesozoic- to Pliocene-aged sediment.		–
Northern Terranes	9–3	AFT, ZrFT, and K-Ar (*45*)	Island-arc volcanics (*31*, *32*) and compressional thrust structures (*45*).	C	–
Papuan Peninsula	12–6	No	–	–	Model exploration for uplift onset is consistent with earliest arc volcanism in region ~12 Ma (*22*).
	6–0	No	–	–	Uplift of the Owen Stanley Ranges attributed to reactivation of the Owen Stanley Fault zone ~6 Ma (*43*, *44*).
Adelbert and Finisterre Terranes	5–0	No	–	–	Terrane accretion estimated at ~4–3.5 Ma (*25*, *46*). Vertical approximation of terrane accretion requires earlier uplift onset to produce elevated topography by the proposed docking time.
Basins	5–0	No	–	–	Uplift imposed from 5 Ma to improve the position of final coastlines. Basin behavior not of study focus.

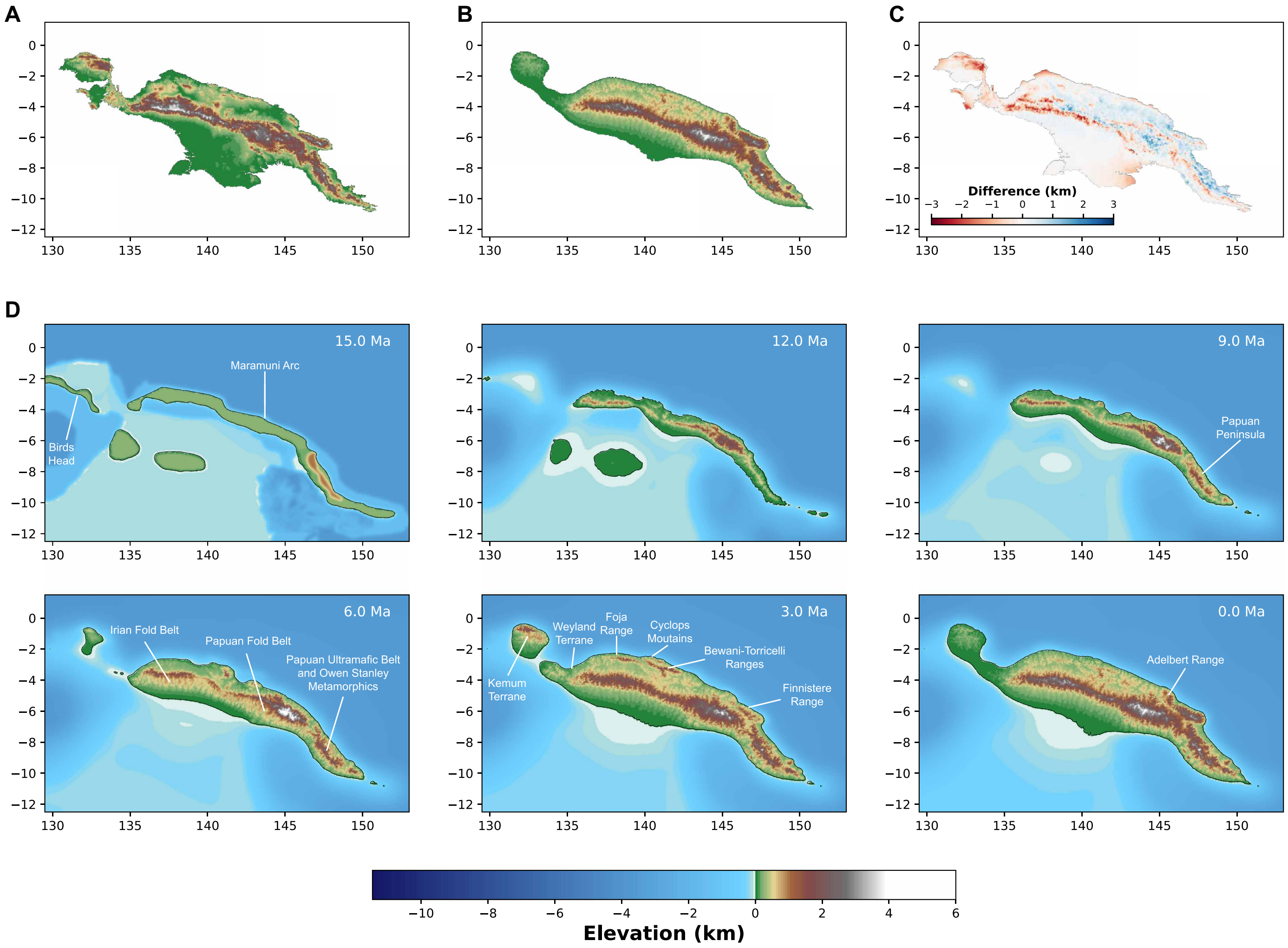

Fig. 2. Comparison of observed and simulated topography and model evolution. (**A**) Regridded New Guinea elevations from the ETOPO Global Relief Model. (**B**) Gridded model topography at the present day. (**C**) Elevation difference between ETOPO and the final simulated topography. (**D**) Simulated topographic evolution from 15 Ma to present. The simulation is initiated with an elevated, elongated region of terrestrial topography, which defines the Maramuni Arc. Key orogenic developments include uplift of the Papuan Peninsula by 9 Ma, emergence of the Bewani-Torricelli Ranges by 6 Ma, southward growth of the Irian and Papuan fold belts, and formation of the Adelbert and Finisterre Ranges by 3 Ma. See movie S1 for the full topographic and erosional evolution.

denudation rates of ~1.2 km/Myr (movie S4). Sediment flux from the eroding highlands contributed to the filling of the deeper bathymetry directly south of the Maramuni Arc between ~15 and 12 Ma, and following the infill of those local depressions around 12 Ma, sediment was transported to the larger Banda Sea and Gulf of Papua basins. Material directed to the northern coast was efficiently transported beyond the narrow shelf and deposited on the slope.

On the Papuan Peninsula, topography was denuded and reduced by <0.7 km (movie S4) between 15 and 12 Ma. During this interval, no tectonic uplift was imposed, but higher elevations were partially sustained by the flexural unloading response arising from denudation. Uplift was imposed along the Papuan Peninsula from 12 Ma, using on the earliest occurrence of arc volcanics to infer a conservative initiation of active tectonism (*22*), at an iteratively determined rate of <0.8 km/Myr (movie S3). This led to the development of 2-km elevations there by 6 Ma. The magnitude of uplift was increased by 25% at 6 Ma to emulate the unzipping of the Papuan Ultramafic Belt ophiolites and associated isostatic rebound (*32*, *43*, *44*), which exposed the Owen Stanley Metamorphics. Erosion of the ranges, at rates of 0.8 to 1.2 km/Myr (movie S4), contributed substantial volumes of sediment to the Gulf of Papua and Solomon Sea (*44*). Furthermore, this period of enhanced uplift caused the ranges along the Papuan Peninsula to connect with the central highlands in the west, forming a continuous range by 5 Ma with individual peaks attaining elevations of 3.0 km.

A 9- to 3-Ma phase of uplift was imposed in north New Guinea to capture the diachronous, west-to-east docking of terranes along the northern margin at that time, as the Proto Solomon Sea–Australian plate boundary transitioned from oblique subduction to transpressional convergence (*24*, *31*, *33*). From west to east, these included the Kemum, Weyland, Foja, Cyclops, and Bewani-Torricelli Terranes. In line with thermochronological evidence (*45*), imposed uplift was maintained along the northern terranes until 3 Ma. Subaerial exposure of the terranes was discernible in the models from 7 Ma, starting with the Bewani-Torricelli and Cyclops Terranes, followed by the Kemum around 6 Ma and the Weyland at 5 to 4 Ma. The modeled topographic expression of the terranes shows an opposite diachronicity to tectonic models, chiefly because the terranes were uplifted together, due to thermochronological and geological data being limited to the Bewani-Torricelli terrane. Lowered topography was observed after 3 Ma following the cessation of imposed uplift. The docking of the Finisterre and Adelbert Terranes to the East was captured by a period of imposed uplift initiating from 5 Ma that continued until the present day, such that the exposure of the terranes matched the estimated ~4.0- to 3.5-Ma timing of accretion (*46*). Sediment eroded from the Finisterre and Adelbert Terranes at rates of ~1.0 to 1.4 km/Myr (movie S4) was routed directly onto the continental slopes and abyssal plain in the Bismarck Sea.

Major physiographic change across the Papuan and Irian fold belts occurred following the southward propagation of uplift from 7 Ma (*22*, *24*, *47*), following the ~8- to 6-Ma transition to transpressional convergence along the northern margin (*24*, *31*, *33*) and plate delamination under the central highlands (*22*, *24*, *47*). Maximum uplift rates occurred south of the preexisting mountains. Uplift consistently ranged between 1.0 and 1.3 km/Myr (movie S3), forming new and taller mountain peaks of up to 5.1 km by present day and extending the thickness of the ranges in a southward direction. At the same time, uplift of the northern components reduced by 70% at 6 Ma, and peaks steadily lowered to elevations below 2.8 km by the present day (*22*, *24*, *31*, *33*, *47*). The Irian and Papuan fold belts formed a continuous range by ~6 Ma. While maximum erosion rates between 7 and 0 Ma were consistently at ~1.5 km/Myr (movie S3), which we attribute to higher elevations and steeper average slopes. Furthermore, erosion was more extensive throughout the Irian Fold Belt from 4 Ma, probably arising from the enhanced rainfall in the west recorded by the integrated paleoclimate model (*40*). Much of the sediment sourced from the highlands was deposited in the southern foreland basin. However, a large portion was transported further into deeper depocenters, such as the Gulf of Papua and the Banda Sea.

Surrounding the Baia deposit along the southern margin of the Papuan Fold Belt (Fig. 1), stratigraphic evidence indicates that the 7-Ma Darai Limestone was regionally uplifted by ~4 to 5 km relative to its burial depth (*48*). Modeled net uplift of 3.8 to 5.5 km (0.5 to 0.8 km/Myr; movie S4) in the Greater Juha area is consistent with this. Near the Grasberg deposit in the Irian Fold Belt (Fig. 1 and table S2), thermochronological data indicate about 7.5 km of uplift since 12 Ma (*28*). Because widespread limestone deposition persisted across New Guinea until 7 Ma (*24*, *31*, *47*), uplift before that time was limited, implying rates of roughly 1 km/Myr thereafter, which match the modeled rates of around 1.4 km/Myr (movie S4). Farther north in Irian Jaya (Hitalipa in table S2), exhumation of the Darai Limestone of ~4 to 7.5 km between 7 and 0 Ma (*49*) aligns with the modeled 6.9 to 7.8 km. Along the older northern Irian Fold Belt, about 11 km of exhumation exposing high-grade Ruffaer Metamorphic rocks (*50*) is consistent with the modeled 12 to 13 km over 15 to 0 Ma (table S2). Lower exhumation magnitudes of 5 to 6 km along the Irian Ophiolite (*50*) also agree with the modeled 4 to 5 km (table S2). Collectively, these results indicate strong agreement between modeled and observed uplift across multiple sites, capturing both the magnitude and spatial gradient of exhumation across New Guinea.

The maximum net uplift rate of ~1.4 km/Myr falls well within the typical range of 1 to 5 km/Myr observed in other convergent margins globally, such as the Andes (*51*, *52*) and the Kiso Range in central Japan (*53*, *54*). Erosion along the frontal slopes of the Irian Fold Belt since 2.3 Ma has been estimated at roughly 1.7 km/Myr (*28*), comparable to modeled rates of 1.1 to 1.2 km/Myr between 2.5 and 0 Ma (movie S4). Predicted denudation rates are also within globally observed values from similar geomorphological settings (0.074 to 4.151 km/Myr) as derived from ^{10}Be cosmogenic radionuclide dating (*29*).

Estimating porphyry ore deposit emplacement depths

Here, we apply Landscape evolution modeling of New Guinea since 15 Ma to show that erosional unroofing is a primary control on the preservation of porphyry copper deposits. For 18 New Guinean porphyry copper ore deposits of known age (*23*, *55*, *56*), emplacement depths were calculated from landscape evolution model exhumation predictions (Figs. 1 and 3 and table S1). Model estimates predict a distinct trend of deeper emplacement with decreasing gold concentration and increasing Cu/Au with increasing emplacement depth that is consistent with global data. Systematic discordance exists between porphyry copper emplacement depths estimated by stratigraphic observations, fluid inclusion data, and our landscape evolution model. Emplacement depth estimates based on stratigraphy systematically suggest shallower paleodepths than fluid inclusion data, while our model predicts the greatest depths by as much as 200 to 400 m. However, close correspondence between predicted emplacement depths and global emplacement depth–copper content trends (Fig. 3) (*57*, *58*) seems to corroborate our postmineralization exhumation model. This is despite the landscape evolution modeling workflow not incorporating local-scale deformation, such as faulting, folding, and lateral translation.

Subsurface porphyry copper prospecting

Discoveries of new porphyry copper ore deposits have steadily diminished over recent decades, in part because most easily found, near-large surface deposits have already been found. Therefore, to meet the rising global demand for Cu and meet the needs of the green energy transition, we require new subsurface exploration techniques. To help fill this technological gap, here, we present an open-source workflow, which combines models that predict the timing and depth of porphyry copper deposit emplacement [in this case, a published machine learning model (movie S2) (*15*)] and landscape evolution modeling to track postmineralization exhumation and preservation. This approach is applicable to other hypogene mineral systems with prior constraints on the depth of emplacement and both spatially and temporally scalable. Using porphyry copper formation predictions (*15*) and an assumed emplacement depth range of 2.0 to 3.25 km based on the emplacement depth distribution for the world's largest porphyry ore deposits (see Materials and Methods), probable areas of high porphyry copper preservation were identified within a conservatively economic mineable depth of 500 m below the surface (Fig. 4).

The spatial distribution of found ore deposits and numerically predicted prospective areas are generally consistent throughout the Irian and Papuan Fold Belts. Mineralization ages throughout those regions are younger than 5 Ma, and model predictions show prospectivity along the Papuan and Irian fold belts and northern Papuan Peninsula, consistent with the localities of known ore deposits.

DISCUSSION

Landscape evolution modeling of New Guinea since 15 Ma demonstrates that integrating multiple tectonic, climatic, and erosional

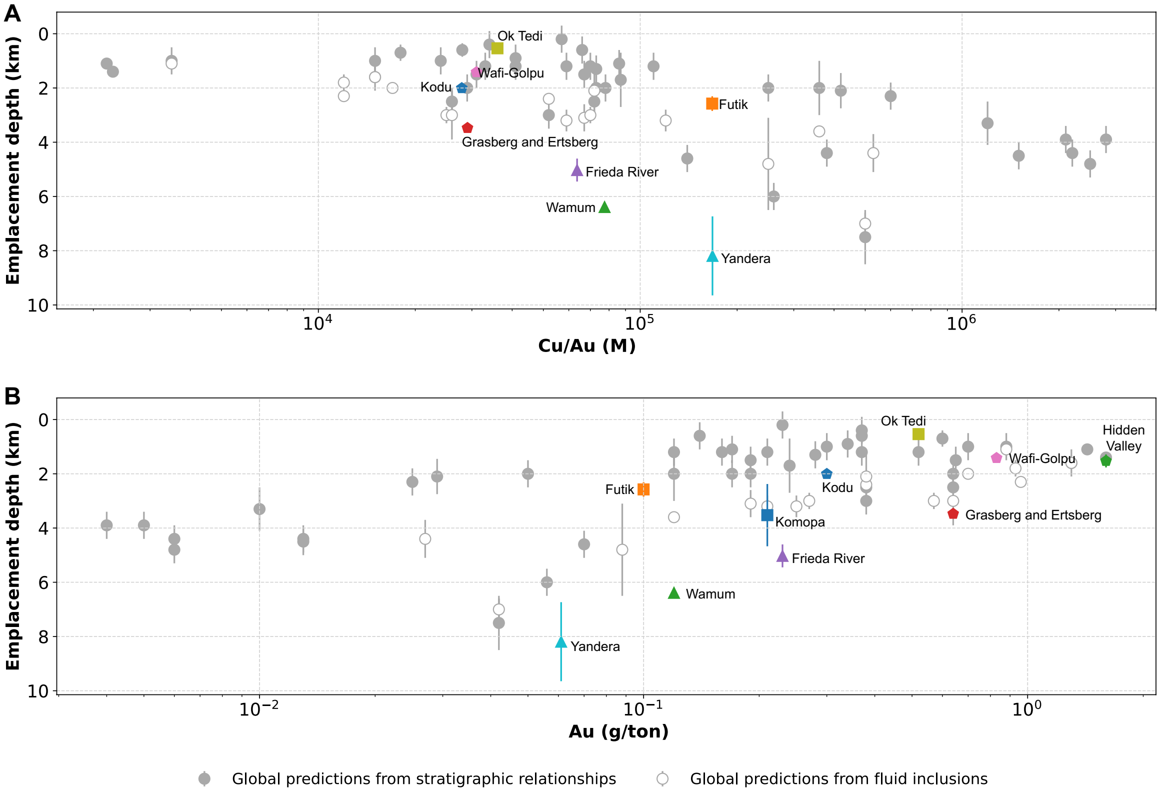

Fig. 3. Geochemical emplacement depth trends between model-derived estimates and global data. (**A**) Estimated emplacement depth and molar ratios of copper to gold. (**B**) Estimated emplacement depth and gold grade. Global estimates are based on geological and stratigraphic constraints or fluid inclusion methods (*57*, *58*). Model-derived estimates (colored squares and triangles) are plotted against their corresponding geochemical data (*23*, *55*), with error bars showing the range of potential emplacement depths due to uncertainty in mineralization ages (*23*, *55*, *56*). Note that only New Guinean porphyry copper deposits with available geochemical data are shown (*57*, *58*).

forcings through an experimental design framework can generate accurate topographic, uplift, and erosional histories. The preferred model yielded relatively accurate present-day topography when compared to ETOPO. The modeled Gulf of Papua depositional volume was ~70% of the empirical evidence, where unmodeled carbonate platform growth would likely contribute most of the missing volume.

The model results also highlight erosional unroofing as a key control on the preservation of ore deposits at the regional scale. Predicted emplacement depths based on modeled erosion match observed values within uncertainty for 5 of 8 ore deposits for Cu/Au, and 8 of 10 deposits for Au (in grams per metric tons) (Fig. 3). The Yandera deposit is within uncertainty for Au (in grams per metric tons) and just outside of uncertainty of Cu/Au, which could relate to a slight overprediction of exhumation.

Notable discordance between emplacement depth predictions is observed for the Frieda River and Wamum ore deposits emplaced at ~12 Ma (*59*) (Figs. 1 and 3). Although the geologically inferred emplacement depth for Frieda River is 2 km (*59*), model predictions suggest depths of 6.2 to 7.3 km. This is likely due to postemplacement burial during a period of compression and overthrusting invoked by authors (*30*, *60*), which was not captured by the modeling workflow. Such a postmineralization history for the Frieda River would help explain its preservation in one of the fastest exhuming active orogens on Earth (*26*–*29*), despite its relatively great antiquity (12 Ma) (*30*, *60*, *61*). Further, we suggest a similar preservation scenario for the Wamum deposit, emplaced at a similar time. In contrast to the Wamum and Frieda River deposits, the prospectivity map (Fig. 4C) indicates that most near-surface porphyry copper ore deposits in New Guinea are younger than 5 Ma. Instead, older deposits, if formed, were for the most part eroded away during extreme Pliocene exhumation, potentially being redeposited elsewhere as sedimentary-hosted deposits.

The results suggest that the Papuan Fold Belt is the most prospective region of New Guinea for near-surface porphyry copper deposits, featuring the highest relative probabilities in abundance. Several pockets of extreme relative likelihood are ~50 to 300 km from found ore deposits and may be helpful to direct and de-risk future greenfield exploration work (141° to 145° E in Fig. 4A). The results suggest that older 15 Ma may be preserved within the southern edge of the Papuan Fold Belt (Fig. 4C). This stems from deposit burial by siliciclastic deposition here between 15 and 7 Ma, followed by uplift and removal of much of the overlying sediment, and exhuming the older ~15-Ma deposits within 500 m of the surface.

The Irian Fold Belt shows high prospectivity in the east but drops to intermediate prospectivity in the west, where the world-class Grasberg ore deposit is hosted (*56*, *59*, *62*). The lower emplacement probabilities in there are due to the predictive porphyry copper emplacement model (*14*), applying a lower weighting toward areas, such as the Irian Fold Belt (movie S2), that have fewer deposits with massive ore tonnage (*58*, *59*). The landscape evolution results suggest

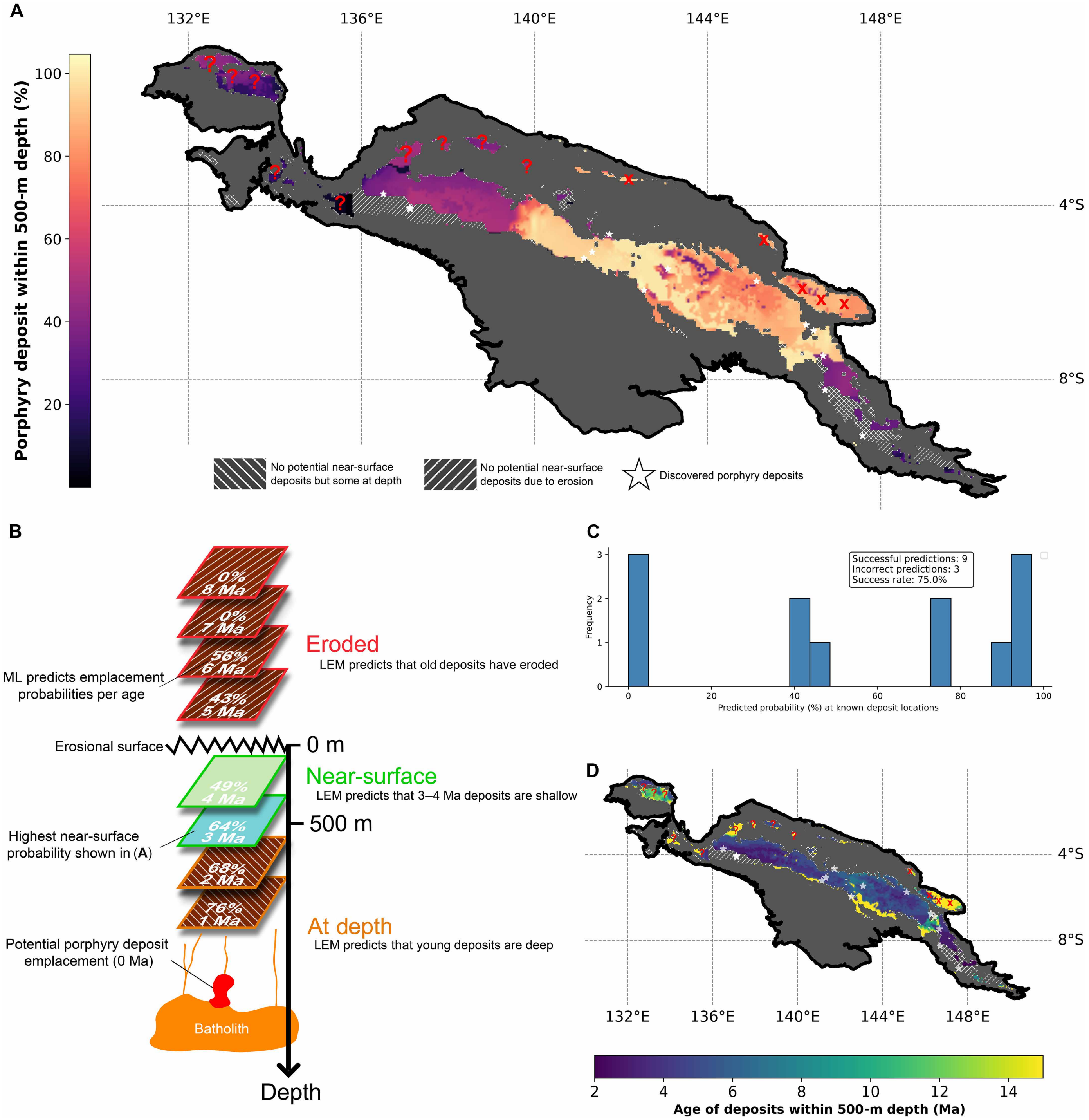

Fig. 4. Predicted near-surface New Guinean porphyry ore deposits. (**A**) Relative likelihood of porphyry copper deposits occurring within 500 m of the surface, based on the integration of spatiotemporal mineralization predictions (*15*) with landscape evolution modeling. Prospectivity was evaluated only in mountainous terrain, defined as regions with elevations above 600 m. Diagonal lines indicate elevated areas where mineralization may have been either eroded or remains deeper than 500 m. (**B**) Schematic of the workflow used to generate (A), which combines modeled erosion histories with mineralization predictions for each cell of the landscape evolution model domain. ML, machine learning. LEM, landscape evolution model. (**C**) Histogram of predicted probabilities at known deposit locations and the corresponding prediction success rate. (**D**) Mineralization ages for predicted high-probability regions shown in (A). Confidence in preservation varies across regions: Predictions in the Foja Range, Weyland Terrane, and Bird's Head are uncertain because of limited calibration data ("?"); predictions in the Adelbert and Finisterre Ranges should be disregarded because of modeling limitations ("×") (see Discussion). Sediment flux data for calibration were extrapolated westward from Papua New Guinea due to lack of local data in West Papua (see Materials and Methods).

that deposits emplaced at depth ~3 Ma are most likely to be preserved near the surface within the Irian Fold Belt (Fig. 4C), which is consistent with the radiometric age for the Grasberg deposit (*62*).

Model predictions in the Papuan Peninsula suggest no near-surface prospectivity surrounding the sites of the ~4.42-Ma Kodu deposit and ~4.9-Ma Ipi River deposit. The recovered emplacement depth for the Kodu deposit is well within expected ranges (Fig. 3), suggesting that the preservation predictions are reliable. Further inspection shows that the formation model predicts no deposit emplacement in the southern Papuan Peninsula between 5 and 4 Ma (*15*). The lack of emplacement stems from the absence of a continent-dipping subduction during this period of the input reconstruction (*35*). The deposits may be postkinematic or related to delamination, often suggested for deposits younger than 7 Ma across New Guinea (*22*–*24*, *31*).

The prospectivity map (Fig. 4A) indicates that near-surface ore deposits throughout the Adelbert and Finisterre Ranges appear to be likely, despite no discoveries yet being made there. Closer inspection shows that preserved mineralization ages in these regions are older than 5 Ma. The regional-scale vertical uplift and denudational focus of our landscape evolution modeling required simplifying the behavior of accreted terranes, including the Bewani-Torricelli, Adelbert, and Finisterre. The horizontal motion of the terranes was simplified to vertical uplift at 5 Ma and emersion above the ocean at 4 Ma. This simplification was incorporated because of computational limitations and poor constraints for the prior paleogeometries and deformation kinematics of these terranes. Therefore, before 4 Ma, the Adelbert and Finisterre Terranes were submerged, rather than offshore terrestrial terranes, and the simulated landscape evolution is locally inconsistent. This suggest that predictions for the preservation of >4-Ma deposits should be disregarded (Fig. 4).

While the uplift of the Bewani-Torricelli Terrane was also simplified, uplift was initiated at 9 Ma, and the western preserved near-surface deposits were emplaced at 6 to 5 Ma. Review of the topography and erosional outputs (Fig. 2 and movies S1 and S4) shows that the erosional behavior had stabilized and geodynamically consistent by 6 Ma for the western Bewani-Torricelli Terrane. Thus, high prospectivity in the west Bewani-Torricelli terrane may warrant further exploration. Contrastingly, predictions for the eastern half are unreliable and highlighted as such in Fig. 4.

Thus, improvements to both the input emplacement prediction model and the landscape evolution simulation could be made to rectify the mismatches between predicted formation ages and known ore deposits in places. For instance, the porphyry copper emplacement model predicts mineralization to occur within the forearc zone of subduction (movie S2). However, in areas such as the Papuan Peninsula, porphyry copper emplacement may not be directly related to active subduction (*23*, *63*). Alternatively, mismatches in mineralization predictions may stem from limitations of the input tectonic reconstruction (*35*).

Landscape evolution models could also be refined with the availability of sediment thickness data from more basins, which would improve model calibration. In particular, the inclusion of data specific to carbonate platform development would allow for the explicit representation of carbonate growth, further enhancing calibration. This would also help address the model's underestimation of total sediment volumes in the Gulf of Papua, which likely stems in part from the exclusion of carbonate deposition. Future work to include deformation through faulting and folding within the models would also likely improve results and resolve some of the outlying emplacement depth estimates. The software capability to include this deformation exists [e.g., underworld modeling code (*64*)]. Still, the computational resource required is currently not feasible for applications running thousands of models with the necessary spatiotemporal resolutions.

Besides these few exceptions, there is broadscale consistency between predicted emplacement depth–tonnage relationships and global geochemical data from other deposits (Fig. 3). The results also indicate several regions with a high likelihood of near-surface porphyry mineralization, including the Papuan Fold Belt, known to host economic porphyry copper deposits, and the Bewani-Torricelli Ranges, a greenfield province (Fig. 4). These results demonstrate that landscape evolution modeling is a powerful tool for quantifying porphyry copper exhumation and preservation potential, even without explicitly simulating structural deformation such as faulting and folding. In contrast to previous conceptual or statistical frameworks (*17*), our physically based, spatially and temporally detailed approach captures complex orogenic processes influencing deposit exposure. When combined with mineralization models that define the time, location, and depth of ore formation, this method enables direct testing of preservation hypotheses and identification of previously unrecognized exploration targets. It offers an adaptable and affordable framework to assist in narrowing the search for greenfield hypogene deposits beyond porphyry copper systems. Hence, this model-based approach can complement and de-risk conventional exploration techniques by treating postmineralization exhumation as a predictive vector. Its open-source implementation promotes broader accessibility across the mining sector, supporting more sustainable and equitable resource development.

MATERIALS AND METHODS

Modeled surface processes

The Badlands (*18*, *65*) landscape evolution model simulates a suite of independent external forcings that affect responsive processes, many of which are interconnected and affect each other. The complex interplaying nature is the reason why these coupled models are required to produce first-order accuracy simulations. Here, we present the responsive processes incorporated in this study. Badlands models topographic change over time using the following

$$\frac{\partial z}{\partial t} = -\nabla \cdot qs + U \tag{1}$$

where $-\nabla \cdot qs$ is the sediment flux and U is the uplift or subsidence. We applied fluvial, marine, and diffusion-based surface processes to model the sediment flux. A transport-limited model was implemented to capture the fluvial incision and transport. Transport-limited models erode material at a rate dependent on the stream power and the load of material already being transported. In general, erosion rates increase for greater load material until a critical point, where further load material progressively impedes erosion rates. The transport limitation is given by $f\left(Q_s\right)$ in Eq. 3. The erosion rate $\dot{\epsilon}_{\text{fluvial}}$ of the transport-limited fluvial model is given as follows

$$\dot{\epsilon}_{\text{fluvial}} = f\left(Q_s\right) Q_s = f\left(Q_s\right) \kappa_d (PA)^m (S)^n \tag{2}$$

where Q_s and its expansion, shown above, are the stream power–dependent erosion rate with parameters: κ_d is the erodibility coefficient, m is the water volume exponent, and n is the slope exponent; and variables: P is the precipitation, A is the upstream catchment area, and S is the channel slope. The function, $f\left(Q_s\right)$, models the transport limitation, which governs the dependence of the net fluvial erosion rate relative to the sediment load. Several plausible approximations for $f\left(Q_s\right)$ were tested, where a parabolic model was found to produce the closest match to the final topography and deposited sediment volumes

$$f\left(Q_s\right)=\begin{cases}1-4\left(\frac{Q_s}{Q_t}-0.5\right)^2, & \frac{Q_s}{Q_t}>0.1\\ 2.6\frac{Q_s}{Q_t}+0.1, & \frac{Q_s}{Q_t}\leq 0.1\end{cases} \tag{3}$$

Q_t is the volumetric sediment transport capacity, given as follows

$$Q_t=\kappa_t(PA)^{m_t}S^{n_t} \tag{4}$$

with additional variables: κ_t is the erodibility of channel sediment, m_t is the transport-limited water volume exponent, and n_t is the transport-limited slope exponent. The hillslope and marine diffusion processes are calculated separately by a simple diffusion law

$$\dot{\epsilon}_{\text{diffusion}}=\kappa_{\text{diff}}\cdot\nabla^2 z \tag{5}$$

where z is the elevation, t is the time, and κ_{diff} is the diffusion coefficient. Two unique κ values are implemented, one for terrestrial settings and the other for marine settings.

Deposition in Badlands can occur under several conditions, including in local topographic depressions (pits), alluvial plains, and marine environments. Topographic depressions are filled by adjacent rivers, governed by a pit-filling algorithm (*66*). Depressions are progressively filled at a rate limited by the available sediment volume in transport, and an upper limit is given by the maximum fill rate parameter ($fillmax = 200$ m/Myr). Alluvial plain deposition occurs at a critical slope (slp_{cr}) along a river (Table 1). The critical slope aims to capture the sharp decrease in the topographic gradient associated with alluvial deposits observed at the foot of a mountain (*67*). Additional restrictions on alluvial deposition are imposed to prevent slope reversals.

Transported sediment that reaches the marine environment is deposited close to the shoreline. Sediment is then moved downslope, governed by a parameter that divides the sediment into equal portions (*diffnb*) (Table 1), which are sequentially moved downslope within a single time step and a second parameter that limits the thickness of deposition relative to neighboring topography (*diffprop*) (Table 1). The two parameters can be altered to produce marine landforms observed in the study area. For example, lower *diffnb* and higher *diffprop* values will create steeper slopes and concentrated nearshore deposition, while increasing *diffnb* will further disperse sediments toward the deep ocean.

We also incorporated sediment compaction into the models. The initial surface porosity value for all lithologies was $\phi_0 = 0.52$ (*18*, *65*), and compaction was modeled by an exponential decay equation (*68*)

$$\phi(d)=\phi_0 e^{-cd}$$

where ϕ is the porosity at depth d (in kilometers), ϕ_0 is the initial surface porosity, and a constant value of $c = 0.47\ \text{km}^{-1}$ was used (*18*, *65*).

We allowed both external forcings and responsive processes contribute to uplift and subsidence (U in Eq. 1). The implemented responsive process was elastic lithospheric flexure due to the loading and unloading of sediment. The response is captured using the gFlex model (*38*), where the effective elastic thickness parameter, T_e, was explored on the basis of estimates for the margin (*69*).

Imposing periods of uplift

Periods of vertical uplift were imposed to implicitly capture the regional-scale topographic response to various processes, such as deformation and crustal thickening related to compression. Simulated uplift was purely vertical, primarily because of the focus of regional-scale vertical unroofing. Several further reasons for not implementing horizontal kinematics were increased computation times and the highly oblique collisional events involving the accretion of island arc terranes that have limited to no constraints on the original geometry, morphology, and deformation during accretion.

The main island of New Guinea was separated into different regions to impose uplift at different times and magnitudes. Region designation was based on the spread of available thermochronological data and estimates for timing of uplift onset and to regions that experienced similar geological events throughout the past 15 Myr (Fig. 5). The onset of uplift in each region (Table 2) was based on the timing of periods of pronounced cooling in published thermal history simulations of thermochronology data, where available. Where studies had supported the interpretation that long-term crustal cooling was due to exhumation based on independent geological data, the onset of cooling was assumed to be roughly coeval with the initiation of an uplift event, and the timing and rate of exhumation were determined from the best-fit cooling paths of thermal history models (Fig. 6). For regions where thermal history models were absent, other lines of evidence were used to estimate the onset of uplift (Table 2).

The imposed uplift was calculated by subtracting the present-day topography from the initial topography, defined as the minimum uplift. During periods of uplift, the minimum uplift was applied with a factor to increase or decrease the uplift. The factors for each region were adjusted throughout the design of experiments phase, such that the models best matched the independent validation data.

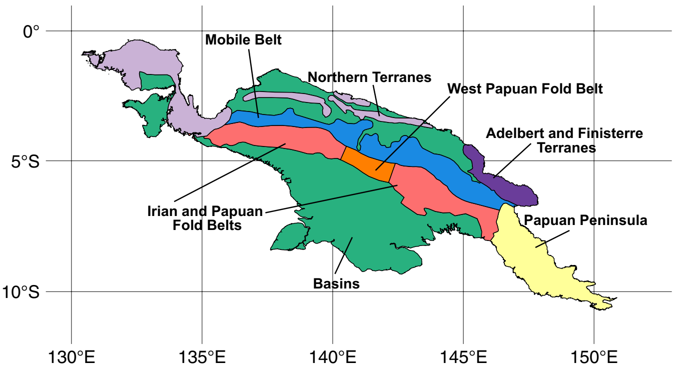

Fig. 5. Region definition to apply spatially and temporally varying uplift. The regions were designated on the basis of data availability and geological similarity within the past 15 Myr. The West Papuan Fold Belt region was separated from the rest of the fold belts, as increased uplift was required to better match the final topography.

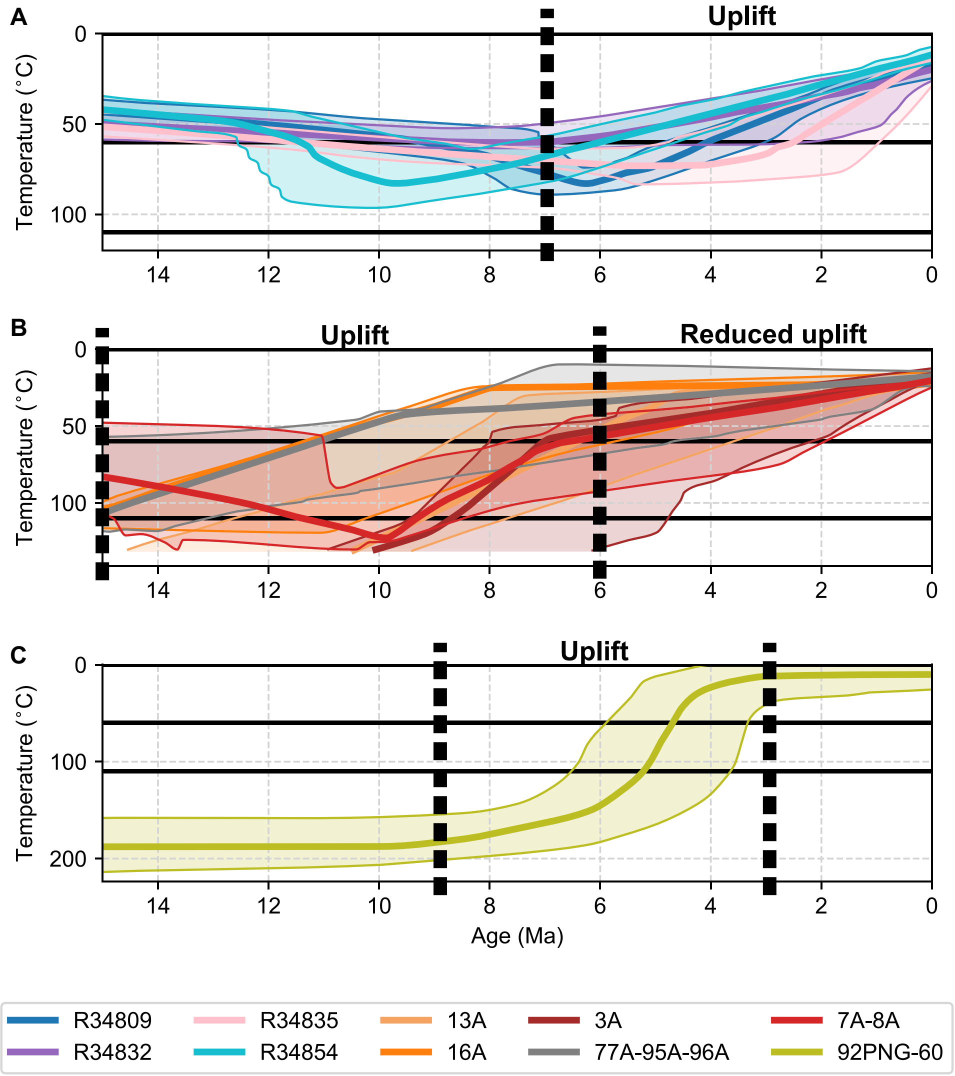

Fig. 6. Timing of uplift events based on published thermal history modeling results of thermochronology data. Dashed black lines delineate periods of uplift, and labels describe the uplift periods and relative rates. Thermal history models developed from samples situated at higher local elevations were preferred, as local depressions, such as valleys, have likely undergone heightened erosion due to fluvial action and do not represent the baseline exhumation history. Shaded envelopes show the 95% confidence interval for statistically plausible time-temperature paths, while solid lines are the best-fit time-temperature path. Models correspond to the regions of the Papuan Fold Belt (**A**) (*72*), Eastern Mobile Belt (**B**) (*33*), and Bewani-Torricelli Ranges (**C**) (*45*).

Initial topography

The initial topography for the main island of New Guinea at the 15-Ma model start time (movie S1) was developed using a revised paleogeographic map, which incorporated a 10-Ma paleogeographic map (*41*) and new constraints on the geological evolution of the margin. Paleogeographic maps (*41*) and inundation maps (*70*) for 20 and 25 Ma support that New Guinea was largely inundated before the model started at 15 Ma. By 10 Ma, the Maramuni Arc was exposed above sea level (*41*, *70*), but crystallization ages for volcanics are as old as ~22 Ma (*22*, *71*), attributed to mark the onset of uplift (*22*, *24*, *31*). Therefore, the exposure of the Maramuni Arc system was justifiably included in the initial topography at 15 Ma. Two elongated islands south of the arc were interpreted by Norvick (*41*) to be the topographic response to the initiation of folding in the Papuan and Irian fold belts. However, Sr isotope and paleontological ages show that widespread Darai limestone deposition lasted until ~7 Ma (*72*), constraining exposure above sea level to post–7 Ma. Thus, the islands were not implemented in the initial topography. Abyssal plain regions were assigned a bathymetry of −5000 m based on observed depths.

The initial topography for the Gulf of Papua was generated using a separate methodology due to the availability of sediment isopachs. The Gulf of Papua sediment thickness data were subtracted from the present-day bathymetry, and the flexural isostatic response of the sediment unloading was calculated using an elastic plate flexure solution (*38*). Input parameters for the flexural unloading were a sediment density of 2511 kg/m^3, based on a present-day composition of ~50% limestone and ~50% sandstone (*73*); a mantle density of 3200 kg/m^3, based on global upper mantle density models (*74*); a margin wide approximation of Young's modulus of 1×10^{11} Pa (*75*); and elastic thickness maps (*69*). A cosine arch smoothing function was then applied to generate the preferred initial topography from the revised paleogeographic map.

Model calibration and validation against independent data

The Python library DoEgen (*20*) and accompanying library Badlands-DoE-Toolset (*21*) were used to generate sets of experiments that contained tens to hundreds of models, allowing for the exploration of multiple parameters. The DoEgen library optimized the number of models and combinations of parameters to most efficiently explore all the desired parameters and values. The Badlands-DoE-Toolset allowed for the streamlined use of the DoEgen library with the Badlands landscape evolution model. In addition, the DoEgen library allowed for the quantitative validation of the models against independent data. The empirical data used for validation included the ETOPO present-day topography resampled to the 5-km grid resolution of the model (*19*) and sediment volumes for the Gulf of Papua. Additional age-coded sediment volumes would improve calibration but are not available for other basins surrounding New Guinea. Validation compared each cell from the model and independent data. The topography validation was based on RMSE between the final model and ETOPO topography, and the sediment validation compared the total volume of sediment in the Gulf of Papua region (Fig. 7).

The explored parameters and values implemented in the preferred model are given in Table 1. Despite the ability to explore several parameters within a single experiment set, an iterative design of experiments (*76*) approach was used, where particular parameters were refined first. Additional parameters were subsequently explored, and the previous parameters were further adjusted. The order of parameter exploration involved implementing the initial estimates for tectonic uplift, initial estimates for a uniform erodibility value, and a detachment-limited fluvial model and values for marine variables from Garrett (*44*). Uplift and erodibility were calibrated to best match the Gulf of Papua deposition volumes and the topography validation data. A transport-limited fluvial model was later implemented, and associated parameters were explored, with erodibility and uplift further adjusted accordingly. Spatially varying erodibility was then implemented on the basis of global relative erodibilities (*39*), marine parameters were further explored, and uplift was again adjusted to improve model performance. The global relative erodibilities are

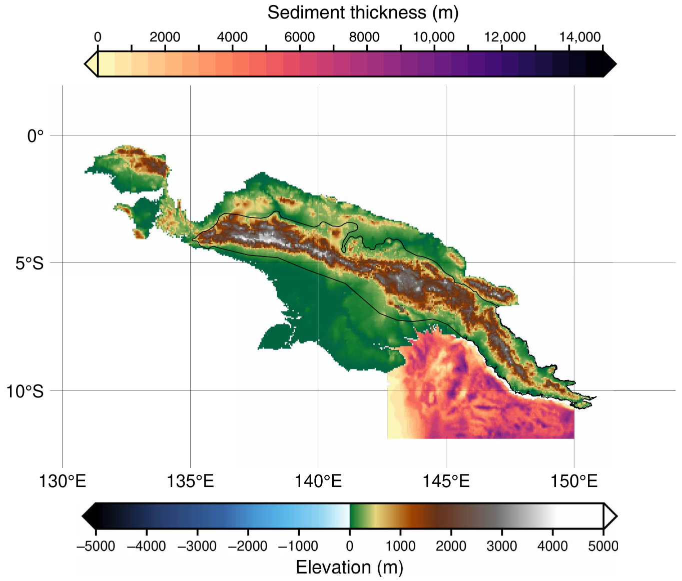

Fig. 7. Present-day topography and sediment thickness data resampled to the model resolution and used for validation tests.

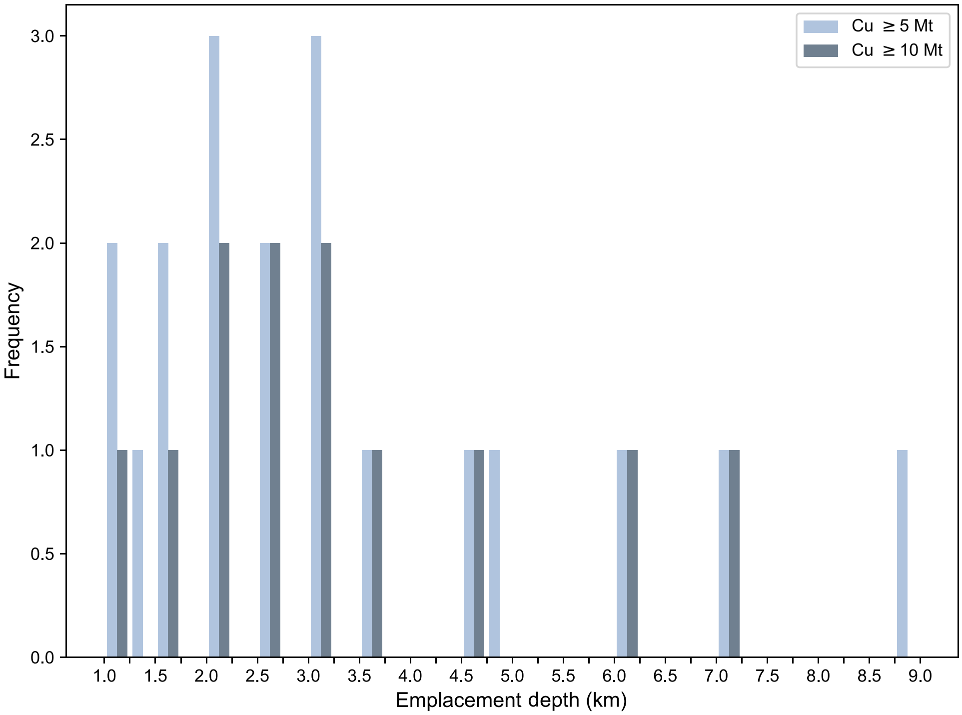

Fig. 8. Common depths of emplacement for large copper ore deposits around the world. A histogram showing the emplacement depth distribution of porphyry copper ore deposits with large tonnage (*58*). A cluster between 1.0 and 3.25 km is discernible, and a more refined cluster is observable between 2.0 and 3.25 km. Mt, million tonnes.

gridded erodibility factors dependent on bedrock lithology (*39*). During calibration, we test various base erodibilities that are then multiplied with the relative factor for each cell within the model domain. These relative erodibilities are static through time, and we justify usage due to the geologically short 15-Myr simulation period.

The experiment sets were run on the Gadi High-Performance Computer, operated by the Australian National Computer Infrastructure. Model runtimes were ~1.5 hours on a single core, and up to 80 models were run simultaneously. Over 2300 models were run to explore the parameter space and to isolate the most dominant processes in the landscape evolution models.

Extraction of unroofing histories

To estimate the emplacement depth of known ore deposits, mineralization ages were used to extract appropriate paleodepths from the preferred landscape evolution model. Paleodepths were determined by subtracting the cumulative erosion at each 500 kyr time step from cumulative erosion at 0 Ma, and a linear interpolation was applied for mineralization ages between paleodepth time intervals.

A framework was developed to predict the likelihood of near-surface preservation for potential porphyry ore deposits. The framework incorporated the calibrated unroofing history extracted from the preferred landscape evolution model and an assumed emplacement depth of 2.0 to 3.25 km (see the "Assumed emplacement depth for large porphyry copper ore deposits" section and Fig. 8) and that near-surface ore deposits were defined as being within 500 m of the surface. The landscape evolution model results and assumptions were used to determine mineralization ages, where ore deposits were predicted to be preserved within 500 m of the surface. The appropriate mineralization ages were then used to filter the spatiotemporal mineralization probability maps (*15*). Where there were multiple possible mineralization ages after filtering, the age with highest emplacement probability was used. Furthermore, the original spatiotemporal mineralization probabilities were filtered to elevations above 600 m, which are typical regions of erosion and porphyry emplacement.

Assumed emplacement depth for large porphyry copper ore deposits

To predict the likelihood of near-surface preservation, an assumed emplacement depth and quantitative definition of near-surface were required. The depths of porphyry copper emplacement globally are typically <3 km but can be as much as 7.5 km (*58*, *59*). However, porphyries emplaced between 2 and 3.25 km have a higher likelihood of greater copper yield globally (Fig. 8). Those bounds were used as the assumed emplacement depth, and near-surface preservation was defined as being within 500 m of the surface.

Supplementary Materials

The PDF file includes:
Tables S1 and S2
Legends for movies S1 to S4

Other Supplementary Material for this manuscript includes the following:
Movies S1 to S4

REFERENCES AND NOTES

1. S. H. Ali, D. Giurco, N. Arndt, E. Nickless, G. Brown, A. Demetriades, R. Durrheim, M. A. Enriquez, J. Kinnaird, A. Littleboy, L. D. Meinert, R. Oberhänsli, J. Salem, R. Schodde, G. Schneider, O. Vidal, N. Yakovleva, Mineral supply for sustainable development requires resource governance. *Nature* **543**, 367–372 (2017).
2. R. Schodde, in *Proceedings of the 11th Fennoscandian Exploration and Mining Conference*, Levi, Finland, 31 October 2017 (MinEx Consulting, 2017), vol. 31.
3. International Energy Agency, *The Role of Critical Minerals in Clean Energy Transitions* (OECD Publishing, 2021).
4. R. Zuo, E. J. M. Carranza, J. Wang, Spatial analysis and visualization of exploration geochemical data. *Earth Sci. Rev.* **158**, 9–18 (2016).
5. M. Abedi, S. A. Torabi, G.-H. Norouzi, M. Hamzeh, ELECTRE III: A knowledge-driven method for integration of geophysical data with geological and geochemical data in mineral prospectivity mapping. *J. Appl. Geophys.* **87**, 9–18 (2012).
6. Q. Yan, L. Xue, Y. Li, R. Wang, B. Wu, K. Ding, J. Wang, Mineral prospectivity mapping integrated with geological map knowledge graph and geochemical data: A case study of gold deposits at Raofeng area, Shaanxi Province. *Ore Geol. Rev.* **161**, 105651 (2023).
7. B. Chudasama, A. Porwal, O. P. Kreuzer, K. Butera, Geology, geodynamics and orogenic gold prospectivity modelling of the Paleoproterozoic Kumasi Basin, Ghana, West Africa. *Ore Geol. Rev.* **78**, 692–711 (2016).
8. A. Joly, A. Porwal, T. C. McCuaig, B. Chudasama, M. C. Dentith, A. R. A. Aitken, Mineral systems approach applied to GIS-based 2D-prospectivity modelling of geological regions: Insights from Western Australia. *Ore Geol. Rev.* **71**, 673–702 (2015).
9. Z. Luo, E. Farahbakhsh, R. D. Müller, R. Zuo, Multivariate statistical analysis and bespoke deviation network modeling for geochemical anomaly detection of rare earth elements. *Appl. Geochem.* **174**, 106146 (2024).
10. J. N. Burkin, M. D. Lindsay, S. A. Occhipinti, E. J. Holden, Incorporating conceptual and interpretation uncertainty to mineral prospectivity modelling. *Geosci. Front.* **10**, 1383–1396 (2019).
11. F. Kohanpour, M. D. Lindsay, S. Occhipinti, W. Gorczyk, Structural controls on proterozoic nickel and gold mineral systems identified from geodynamic modelling and geophysical interpretation, east Kimberley, Western Australia. *Ore Geol. Rev.* **95**, 552–568 (2018).
12. S. Cloetingh, J. D. van Wees, P. A. Ziegler, L. Lenkey, F. Beekman, M. Tesauro, A. Förster, B. Norden, M. Kaban, N. Hardebol, D. Bonté, A. Genter, L. Guillou-Frottier, M. Ter Voorde, D. Sokoutis, E. Willingshofer, T. Cornu, G. Worum, Lithosphere tectonics and thermo-mechanical properties: An integrated modelling approach for Enhanced Geothermal Systems exploration in Europe. *Earth Sci. Rev.* **102**, 159–206 (2010).
13. N. Butterworth, D. Steinberg, R. D. Müller, S. Williams, A. S. Merdith, S. Hardy, Tectonic environments of South American porphyry copper magmatism through time revealed by spatiotemporal data mining. *Tectonics* **35**, 2847–2862 (2016).
14. J. Diaz-Rodriguez, R. D. Müller, R. Chandra, Predicting the emplacement of Cordilleran porphyry copper systems using a spatio-temporal machine learning model. *Ore Geol. Rev.* **137**, 104300 (2021).
15. E. Farahbakhsh, S. Zahirovic, B. McInnes, S. Polanco, F. Kohlmann, M. Seton, R. D. Müller, Machine learning-based spatio-temporal prospectivity modeling of porphyry systems in the New Guinea and Solomon Islands Region. *Tectonics* **44**, e2024TC008362 (2025).
16. Z. Zhang, G. Wang, E. J. M. Carranza, J. Fan, X. Liu, X. Zhang, Y. Dong, X. Chang, D. Sha, An integrated framework for data-driven mineral prospectivity mapping using bagging-based positive-unlabeled learning and Bayesian cost-sensitive logistic regression. *Nat. Resour. Res.* **31**, 3041–3060 (2022).
17. B. J. Yanites, S. E. Kesler, A climate signal in exhumation patterns revealed by porphyry copper deposits. *Nat. Geosci.* **8**, 462–465 (2015).
18. T. Salles, X. Ding, G. Brocard, pyBadlands: A framework to simulate sediment transport, landscape dynamics and basin stratigraphic evolution through space and time. *PLOS ONE* **13**, e0195557 (2018).
19. ETOPO 2022 15 Arc-Second Global Relief Model, NOAA National Centers for Environmental Information (2022).
20. S. Haan, C. Howden, D. Azam, J. Nothman, D. Müller, M. Boyd, DoEgen: A Python Library for Optimised Design of Experiment Generation and Evaluation (Sydney Informatics Hub, University of Sydney, 2021); https://github.com/sebhaan/DoEgen.
21. M. Boyd, Badlands-Doe-Toolset (Sydney Informatics Hub, University of Sydney, 2023); https://10.5281/zenodo.10892653.
22. R. J. Holm, C. Spandler, S. W. Richards, Continental collision, orogenesis and arc magmatism of the Miocene Maramuni Arc, Papua New Guinea. *Gondwana Res.* **28**, 1117–1136 (2015).
23. R. J. Holm, S. Tapster, H. A. Jelsma, G. Rosenbaum, D. F. Mark, Tectonic evolution and copper-gold metallogenesis of the Papua New Guinea and Solomon Islands region. *Ore Geol. Rev.* **104**, 208–226 (2019).
24. S. Zahirovic, K. J. Matthews, N. Flament, R. D. Müller, K. C. Hill, M. Seton, M. Gurnis, Tectonic evolution and deep mantle structure of the eastern Tethys since the latest Jurassic. *Earth Sci. Rev.* **162**, 293–337 (2016).
25. L. D. Abbott, E. A. Silver, R. S. Anderson, R. Smith, J. C. Ingle, S. A. Kling, D. Haig, E. Small, J. Galewsky, W. S. Sliter, Measurement of tectonic surface uplift rate in a young collisional mountain belt. *Nature* **385**, 501–507 (1997).

26. L. G. Mahoney, "The structure and evolution of the northern Australian margin: Insights from the Papuan Fold and Thrust Belt, Papua New Guinea," thesis, University of Melbourne (2021).
27. D. M. Alongi, P. Christoffersen, F. Tirendi, A. I. Robertson, The influence of freshwater and material export on sedimentary facies and benthic processes within the Fly Delta and adjacent Gulf of Papua (Papua New Guinea). *Cont. Shelf Res.* **12**, 287–326 (1992).
28. R. J. Weiland, M. Cloos, Pliocene-Pleistocene asymmetric unroofing of the Irian fold belt, Irian Jaya, Indonesia: Apatite fission-track thermochronology. *Geol. Soc. Am. Bull.* **108**, 1438–1449 (1996).
29. H. Hecht, T. Oguchi, Global evaluation of erosion rates in relation to tectonics. *Prog Earth Planet Sci* **4**, 40 (2017).
30. K. Hill, R. Kendrick, P. Crowhurst, P. Gow, Copper-gold mineralisation in New Guinea: Tectonics, lineaments, thermochronology and structure. *Aust. J. Earth Sci.* **49**, 737–752 (2002).
31. K. Hill, R. Hall, "Mesozoic-Cenozoic evolution of Australia's New Guinea margin in a west Pacific context," in *Evolution and Dynamics of the Australian Plate* (Geological Society of America, 2003), pp. 265–290.
32. H. L. Davies, The geology of New Guinea - the cordilleran margin of the Australian continent. *Episodes* **35**, 87–102 (2012).
33. K. C. Hill, A. Raza, Arc-continent collision in Papua Guinea: Constraints from fission track thermochronology. *Tectonics* **18**, 950–966 (1999).
34. G. Bárdossy, J. Fodor, Traditional and new ways to handle uncertainty in geology. *Nat. Resour. Res.* **10**, 179–187 (2001).
35. R. D. Müller, S. Zahirovic, S. E. Williams, J. Cannon, M. Seton, D. J. Bower, M. G. Tetley, C. Heine, E. Le Breton, S. Liu, S. H. J. Russell, T. Yang, J. Leonard, M. Gurnis, A global plate model including lithospheric deformation along major rifts and orogens since the Triassic. *Tectonics* **38**, 1884–1907 (2019).
36. M. Seton, S. E. Williams, M. Domeier, A. S. Collins, K. Sigloch, Deconstructing plate tectonic reconstructions. *Nat. Rev. Earth Environ.* **4**, 185–204 (2023).
37. K. G. Miller, J. V. Browning, W. J. Schmelz, R. E. Kopp, G. S. Mountain, J. D. Wright, Cenozoic sea-level and cryospheric evolution from deep-sea geochemical and continental margin records. *Sci. Adv.* **6**, eaaz1346 (2020).
38. A. D. Wickert, Open-source modular solutions for flexural isostasy: gFlex v1.0. *Geosci. Model Dev.* **9**, 997–1017 (2016).
39. N. Moosdorf, S. Cohen, C. von Hagke, A global erodibility index to represent sediment production potential of different rock types. *Appl. Geogr.* **101**, 36–44 (2018).
40. P. J. Valdes, C. R. Scotese, D. J. Lunt, Deep ocean temperatures through time. *Clim. Past* **17**, 1483–1506 (2021).
41. M. S. Norvick, New Palaeogeographic Maps of the northern margins of the Australian plate - Updated report (Geoscience Australia, 2003).
42. E. Löffler, *Geomorphology of Papua New Guinea* (Commonwealth Scientific and Industrial Research Organization in association with Australian National University Press, 1977).
43. C. Pain, Volcanic rocks and surfaces as indicators of Landform Age: The astrolabe agglomerate, Papua New Guinea. *Aust. Geogr.* **15**, 376–381 (1983).
44. R. P. Garrett, "Constraining upland erodibility and marine deposition: Source-to-sink sediment transfer in the Gulf of Papua", thesis, University of Sydney (2020).
45. P. V. Crowhurst, K. C. Hill, D. A. Foster, A. P. Bennett, Thermochronological and geochemical constraints on the tectonic evolution of northern Papua New Guinea. *Geol. Soc. Spec. Publ.* **106**, 525–537 (1996).
46. L. D. Abbott, E. A. Silver, P. R. Thompson, M. V. Filewicz, C. Schneider, Abdoerrias, Stratigraphic constraints on the development and timing of arc-continent collision in northern Papua New Guinea. *J. Sediment. Res.* **64**, 169–183 (1994).
47. M. Cloos, B. Sapiie, A. Ufford, R. Weiland, P. Warren, T. McMahon, "Collisional delamination in New Guinea: The geotectonics of subducting slab breakoff," in *Collisional Delamination in New Guinea: The Geotectonics of Subducting Slab Breakoff* (Geological Society of America, 2005), vol. 400, pp. 1–51.
48. L. Mahoney, K. Hill, S. McLaren, A. Hanani, Complex fold and thrust belt structural styles: Examples from the Greater Juha area of the Papuan Fold and Thrust Belt, Papua New Guinea. *J. Struct. Geol.* **100**, 98–119 (2017).
49. P. Q. Warren, M. Cloos, Petrology and Tectonics of the Derewo Metamorphic Belt, West New Guinea. *Int. Geol. Rev.* **49**, 520–553 (2007).
50. R. J. Weiland, "Emplacement of the Irian ophiolite and unroofing of the Ruffaer metamorphic belt of Irian Jaya, Indonesia," thesis, The University of Texas at Austin (1999).
51. K. M. Gregory-Wodzicki, Uplift history of the Central and Northern Andes: A review. *Geol. Soc. Am. Bull.* **112**, 1091–1105 (2000).
52. M. T. Ramírez-Herrera, K. Gaidzik, S. L. Forman, Spatial variations of tectonic uplift - Subducting plate effects on the Guerrero Forearc, Mexico. *Front. Earth Sci.* **8**, doi.org/10.3389/feart.2020.573081 (2021).
53. S. Sueoka, B. P. Kohn, T. Tagami, H. Tsutsumi, N. Hasebe, A. Tamura, S. Arai, Denudation history of the Kiso Range, central Japan, and its tectonic implications: Constraints from low-temperature thermochronology. *Isl. Arc* **21**, 32–52 (2012).
54. S. Sueoka, H. Tsutsumi, T. Tagami, New approach to resolve the amount of Quaternary uplift and associated denudation of the mountain ranges in the Japanese Islands. *Geosci. Front.* **7**, 197–210 (2016).
55. Minerba One Map Indonesia. Ministry of Energy and Mineral Resources, Indonesia (Indonesia, 2021); https://momi.minerba.esdm.go.id/.
56. S. Wafforn, S. Seman, J. Kyle, D. Stockli, C. Leys, D. Sonbait, M. Cloos, Andradite garnet U-Pb geochronology of the big Gossan skarn, Ertsberg-Grasberg mining district, Indonesia. *Econ. Geol.* **113**, 769–778 (2018).
57. M. Chiaradia, Gold endowments of porphyry deposits controlled by precipitation efficiency. *Nat. Commun.* **11**, 248 (2020).
58. H. Murakami, J. H. Seo, C. A. Heinrich, The relation between Cu/Au ratio and formation depth of porphyry-style Cu–Au ± Mo deposits. *Miner. Deposita* **45**, 11–21 (2010).
59. D. A. Singer, V. I. Berger, B. C. Moring, *Porphyry Copper Deposits of the World: Database and Grade and Tonnage Models, 2008*" (US Geological Survey, 2008).
60. P. Crowhurst, K. Hill, D. Foster, G. Hancock, in Proceedings of the Papua New Guinea Geology, Exploration and Mining Conference. Australasian Institute of Mining andMetallurgy (1997), pp. 51–60.
61. B. I. A. McInnes, K. A. Farley, R. H. Sillitoe, B. P. Kohn, Application of apatite (U-Th)/He thermochronometry to the determination of the sense and amount of vertical fault displacement at the Chuquicamata porphyry copper deposit, Chile. *Econ. Geol.* **94**, 937–947 (1999).
62. S. Wafforn, M. Cloos, D. F. Stockli, "Geo- and thermochronology of the Ertsberg-Grasberg Cu-Au mining district, west New Guinea, Indonesia," thesis, The University of Texas at Austin (2017).
63. R. J. Holm, G. Rosenbaum, S. W. Richards, Post 8Ma reconstruction of Papua New Guinea and Solomon Islands: Microplate tectonics in a convergent plate boundary setting. *Earth Sci. Rev.* **156**, 66–81 (2016).
64. J. Mansour, J. Giordani, L. Moresi, R. Beucher, O. Kaluza, M. Velic, R. Farrington, S. Quenette, A. Beall, Underworld2: Python geodynamics modelling for desktop, HPC and cloud. *J. Open Source Softw.* **5**, 1797 (2020).
65. T. Salles, Badlands: A parallel basin and landscape dynamics model. *SoftwareX* **5**, 195–202 (2016).
66. O. Planchon, F. Darboux, A fast, simple and versatile algorithm to fill the depressions of digital elevation models. *Catena* **46**, 159–176 (2002).
67. P. A. Allen, *Sediment Routing Systems: The Fate of Sediment from Source to Sink* (Cambridge Univ. Press, 2017).
68. L. F. Athy, Density, porosity, and compaction of sedimentary rocks. *AAPG Bull.* **14**, 1–24 (1930).
69. M. Tesauro, M. K. Kaban, S. A. P. L. Cloetingh, Global strength and elastic thickness of the lithosphere. *Global Planet. Change* **90-91**, 51–57 (2012).
70. L. Harrington, S. Zahirovic, N. Flament, R. D. Müller, The role of deep Earth dynamics in driving the flooding and emergence of New Guinea since the Jurassic. *Earth Planet. Sci. Lett.* **479**, 273–283 (2017).
71. Papua New Guinea 1:250 000 geological series. Australian Bureau of Mineral Resources, Geology and Geophysics (Geological Survey of Papua New Guinea, 1968); https://nla.gov.au/nla.obj-233559620.
72. L. Mahoney, S. McLaren, K. Hill, B. Kohn, K. Gallagher, M. Norvick, Late Cretaceous to Oligocene burial and collision in western Papua New Guinea: Indications from low-temperature thermochronology and thermal modelling. *Tectonophysics* **752**, 81–112 (2019).
73. R. D. Müller, J. Cannon, S. Williams, A. Dutkiewicz, PyBacktrack 1.0: A tool for reconstructing paleobathymetry on oceanic and continental crust. *Geochem. Geophys. Geosyst.* **19**, 1898–1909 (2018).
74. R. Tenzer, M. Bagherbandi, P. Vajda, Global model of the upper mantle lateral density structure based on combining seismic and isostatic models. *Geosci. J.* **17**, 65–73 (2013).
75. D. Haddad, A. B. Watts, Subsidence history, gravity anomalies, and flexure of the northeast Australian margin in Papua New Guinea. *Tectonics* **18**, 827–842 (1999).
76. P. Goos, B. Jones, *Optimal Design of Experiments: A Case Study Approach* (Wiley, ed. 1. Aufl., 2011).
77. K. C. Hill, A. J. Gleadow, Apatite fission track analysis of the Papuan Basin. Papua New Guinea (PNG) Petroleum Convention Proceedings. PNG Chamber of Mines and Petroleum (1990), pp. 119-136.
78. K. C. Hill, A. J. W. Gleadow, Uplift and thermal history of the Papuan Fold Belt, Papua New Guinea: Apatite fission track analysis. *Aust. J. Earth Sci.* **36**, 515–539 (1989).
79. R. W. Page, Geochronology of igneous and metamorphic rocks in the New Guinea Highlands. Australian Bureau of Mineral Resources, Geology and Geophysics (1976), pp. 95-101.

Acknowledgments

Funding: This work was supported by Sydney Informatics Hub, a Core Research Facility of the University of Sydney (to A.T., S.Z., and S.P.); National Computational Infrastructure (NCI), which is supported by the Australian government (to A.T. and S.Z.); Australian Research Council grant

DE210100084 (to S.Z.); and PLATO Australian Research Council Linkage project LP210100173 (to A.T., S.Z., S.P., F.K., M.S., and D.R.M.). **Author contributions:** Conceptualization: A.T., S.Z., S.P., B.M., L.M., C.M., F.K., and M.S. Methodology: A.T., S.Z., M.B., S.P., C.M., T.S., P.R., Y.I., B.M., S.C.B., E.F., and F.K. Investigation: A.T., S.Z., S.P., S.C.B., L.M., B.M., and P.R. Visualization: A.T. and S.P. Supervision: S.Z., S.P., S.C.B., L.M., B.M., and D.R.M. Writing—original draft: A.T., S.Z., and S.P. Writing—review and editing: A.T., S.Z., S.P., C.M., S.C.B., P.R., Y.I., L.M., T.S., B.M., F.K., E.F., M.S., and D.R.M. **Competing interests:** The authors declare that they have no competing interests. **Data and materials availability:** The model input data and additional are available at https://zenodo.org/records/15867083. Available data include the inputs for the preferred Badlands landscape evolution model, the external data used for model calibration (topography and sediment thickness), the global geochemical–emplacement depth data in Fig. 3, global emplacement depth and deposit size data in Fig. 5, and machine learning emplacement predictions in Fig. 4. Thermal models are available in the original articles, as referenced. The three-dimensional maps in Fig. 1 were created with the open-source ParaView software (www.paraview.org), and Generic Mapping Tools (www.generic-mapping-tools.org) was used for the two-dimensional map visualization in Fig. 2. A series of Jupyter notebooks are available at https://zenodo.org/records/15867083. The notebooks allow users to compute the preferred model or the entire experiment set from which the preferred model was selected (including the validation of the models against the external data). Further notebooks are provided for the visualization of the Badlands landscape evolution model, the generation of emplacement depth predictions and comparison to global data in Fig. 3, the emplacement depth and deposit size histogram in Fig. 5, and a Python-based version of the near-surface deposit prospectivity map in Fig. 4A.

Submitted 29 April 2025
Accepted 29 October 2025
Published 26 November 2025
10.1126/sciadv.ady6244